SPE 124974

Predicting Relative-Permeability Curves Directly From Rock Images

Dmitriy Silin, SPE, Lawrence Berkeley National Laboratory, and Tad Patzek, SPE, University of Texas, Austin

This paper was prepared for presentation at the 2009 SPE Annual Technical Conference and Exhibition held in New Orleans, Louisiana, USA, 4-7 October 2009.

Abstract

The objective of this study is determination of relative permeability curves from an analysis of the pore space geometry. The main assumptions are that the capillary pressure determines the fluid distribution and the rock is water-wet. Maximal inscribed spheres computations characterize the portion of the pore space occupied by each fluid at a given saturation. Numerical solution of the Stokes equations evaluates the pore-scale flow field, which is averaged to estimate the permeability to each fluid. The computed relative permeability curves are in good agreement with published data.

The input for the proposed procedure can be either a computer tomography image of a sample of the rock of interest, or a computer-generated image based on depositional simulations. Partitioning of the entire domain into parts significantly improves the convergence and makes feasible implementation of the computational procedure on a desktop computer. The stability of the results with respect to the choice of computational parameters makes the proposed method suitable for routine applications. The model admits generalizations relaxing the requirement of water wetness of the rock. This model can be applied to evaluate the evolution of the rock flow properties under deformation, damage, mineral dissolution and precipitation.

Introduction

Flow properties of natural rocks or other porous media are ultimately determined by the pore space geometry and connectivity. Laboratory core experiments are the main tool for studying these properties for scientific and practical applications. High-resolution rock images and computing power allow direct computation of rock transport properties that complement and guide laboratory experiments.

Flow simulations on 3D images of the pore space provide valuable insights into the fundamental physics of Darcy flow. Comprehensive models and efficient computational algorithms make simulated experiments a powerful tool with strong predictive capabilities. Various scenarios of fluid displacement in different wettability conditions can be tried on numerous images with very limited participation of technical personnel. In some situations, as in the case of loosely consolidated formation, reliable measurements are practically impossible, and computer simulations are the only alternative.

Literature presents a number of pore-scale studies of fluid flow. Fatt [1–3] had pointed out the importance of cross-flow between the voids in the pore space. Instead of the model of a bundle of capillary tubes, which was routinely used before, Fatt proposed a pore-network model. He had demonstrated that a simple-geometry network of tubes is capable of capturing the essential features of the flow in a porous medium and of providing valuable insights into the underlying microscopic mechanisms. However, a generic network does not necessarily reflect the pore space geometry of a particular rock of interest. Øren with co-workers [4] have extended flow simulations to unstructured networks derived from the three-dimensional tomography images of the pore space of natural rocks. The association of the network-based simulations with the specific rock data made possible to speak of “predictive capabilities” of the pore-scale modeling approach [5]. Numerous studies have been conducted to simulate two- or three-phase flows and model the impact of wettability, the displacement hysteresis, *etc*. [6–11].

The major computational advantage of the pore network approach is the simplified treatment of Darcy flow. The flow in the entire network sums up from Poiseuille-type flows in the individual channels, called pore throats. In the pore bodies, which are the junctions of multiple throats, the mass balance equations yield an analog of the Kirchhoff’s first rule. A Poiseuille-type solution to the steady-state Navier–Stokes equations implies straightforward rules describing the hydraulic conductance of a flow channel with a relatively simple cross-section geometry [12, 13]. A more complex geometry may significantly complicate description of the conductance [14].

Despite all the simplifying assumptions, pore-network modeling has proved to be a useful tool providing insights into the physics and micromechanics of fluid flow in porous media. Comprehensive overviews of the pore-network approach over the past five decades can be found in [15, 16]. However, the problem of generating a network reflecting the specific properties of a given porous medium still remains art and challenge; no universal routine procedure is available. To bypass the challenges associated with extraction of a representative

network, one can simulate fluid flow directly on a 3D image of the pore space. This approach necessitates solving flow equations on a 3D domain of extremely complex geometry. One group of numerical simulations relies on the Lattice-Boltzmann method [17–21]. This method utilizes the basic physics and is rather universal within the range of phenomena suitable for numerical simulations. At the same time, a rigorous formulation of no-slip or fixed-pressure boundary conditions may be not as simple [22–24]. Lattice-Boltzmann simulations of two-phase flow, accounting for the interfacial phenomena, require massive computations. The increment of complexity of the Lattice-Boltzmann calculations of single- and two-phase flow in porous media is gigantic.

The finite-difference approach to simulation of the fluid flow in the pore space has been used for a long time [25–28], and we employ this approach here. It makes possible incorporation of a wide variety of boundary conditions. The assumption is that the flow is steady and slow (creeping). Thus, the time derivative and the convective term in the flow equations can be dropped. At the microscopic scale of a computer-tomography image, the compressibility of the fluid can be neglected as well, which yields a linear system of Stokes' equations. To simulate two-phase flow at a pore scale, we combine a finite-differences discretization of the Stokes equations with the Maximal Inscribed Spheres (MIS) algorithm [29–31]. MIS-calculations employ simple rules and efficient cluster search algorithms [32], so that the simulations require a modest computer power. All simulations presented in this study have been perform on a desktop personal computer.

An X-ray microtomography-based digital image is a set of cubic voxels. Each voxel is either void or solid. The void voxels describe the pore space geometry and can be naturally used for a spacial discretization of the differential equations that govern fluid flow and their boundary conditions. The image resolution determines the dimensions of each voxel. A high-resolution image describes the pore-space geometry in a greater detail. However, the large size of computational domain may complicate flow simulations. For instance, a digital image of dimensions $100 \times 100 \times 100$ voxels is quite small from the point of view of representative high-resolution imaging. However, it requires solution of a boundary-value problem on hundreds of thousands of grid cells. The matrix of the discretized incompressible flow equations is non-symmetric and the convergence of the numerical solution can be quite slow. Rigorous theoretical estimates of the convergence of a numerical solution to the exact one are available for very few idealized situations. To figure out the computational parameters yielding reasonable accuracy of the simulations, we use test problems with known exact solutions.

In single phase flow, both the finite differences algorithms and the Lattice-Boltzmann method lead to numerical solutions to the Stokes equations. Apparently there is no obvious winner between the two approaches. Some finite-difference and Lattice-Boltzmann numerical schemes are very close to each other [33].

In the numerical simulations within this study, we employ the method of artificial compressibility developed originally by Chorin [34]. This method focuses on steady-state solutions, where the time-evolution of the flow is not of interest. We combine this approach with partitioning the entire digital image into parts. This partitioning helps to reduce the computations. The parts are layers with the lateral dimensions much larger than the depth. The permeability of the entire sample is evaluated by the harmonic mean of the permeabilities of the individual parts.

Prediction of the absolute permeability still remains uncertain due to the heterogeneity of the rock and, consequently, the high variability of the results. However, evaluation of the relative permeabilities is based on the ratio of the permeability to each fluid and the absolute permeability. The partitioning of the sample allows for solving flow equations with high accuracy. A combination of flow simulations with Maximal Inscribed Spheres calculations provides an opportunity to compute relative permeability curves. It turns out that MIS calculations are an efficient way of generating realistic capillary pressure curves [35, 36]. It also turns out that the MIS-computed relative permeability curves are in agreement with coreflood measurements.

This paper is organized as follows. First, we briefly overview the method of artificial compressibility of solving the steady-state Stokes' equations. Second, we describe the discretization and the numerical algorithm and verify the adequate convergence requirements. After that, we present a procedure for evaluating the absolute and relative permeabilities from a tomography image by partitioning that image into layers. Finally, we summarize the findings and conclusions.

The method of artificial compressibility

In this section, we describe an implementation of the method of artificial compressibility [34]. Navier-Stokes equations for flow of a viscous incompressible fluid have the form

$$\frac{\partial}{\partial t}\mathbf{v} + (\mathbf{v}\cdot\nabla)\mathbf{v} = -\frac{1}{\varrho}\nabla p + \nu\nabla^2\mathbf{v} + \mathcal{F} \tag{1}$$

$$\nabla\cdot\mathbf{v} = 0 \tag{2}$$

see [37]. Here $\mathbf{v} = (v_x, v_y, v_z)$ is the local velocity of the fluid flow, p and ϱ are the fluid pressure and density, ν is the coefficient of kinematic viscosity. We neglect the gravity or any other body forces, that is, $\mathcal{F} = 0$. In dimensionless variables:

$$\mathbf{v}' = \frac{\mathbf{v}}{V}, \quad \mathbf{r}' = \frac{\mathbf{r}}{D}, \quad p' = \frac{Dp}{\varrho_0\nu V}, \quad t' = \frac{\nu}{D^2}t \tag{3}$$

where V and D are some characteristic velocity and distance scales, Equations (1) take on the form

$$\frac{\partial}{\partial t'}\mathbf{v}' + \mathrm{Re}(\mathbf{v}'\cdot\nabla)\mathbf{v}' = -\nabla p' + \nabla^2\mathbf{v}' \tag{4}$$

Here

$$\mathrm{Re} = \frac{VD}{\nu} \tag{5}$$

is the Reynolds number. Below, we will skip the prime in order to avoid cumbersome notations. The idea of the artificial compressibility method is as follows: we replace the Navier–Stokes equations for an incompressible flow with a system of equations

$$\frac{\partial}{\partial t}\mathbf{v} + \mathrm{Re}(\mathbf{v}\cdot\nabla)\mathbf{v} = -\nabla p + \nabla^2\mathbf{v} \tag{6}$$

$$\frac{\partial \rho}{\partial t} + \nabla\cdot\mathbf{v} = 0 \tag{7}$$

where ρ is a dimensionless density. A linear relationship between the dimensionless pressure and the artificial density

$$\rho = \delta p \tag{8}$$

describes the compressibility. Both, the dimensionless density, ρ, and the artificial compressibility factor, δ, are not physical quantities, but computational parameters. Their values are to be chosen to facilitate the computations. If a solution to equations (6)–(7) converges to a steady solution as $t \to \infty$, then the time derivatives, including the one in Equation (7), vanish, and one obtains a steady-state solution for incompressible flow. Note that this limiting steady-state solution depends neither on ρ, nor on δ. At any given t, the magnitudes of the time derivatives in Equations (6) and (7) actually evaluate the approximation to the steady flow equation.

Our objective is steady-state creeping flow, where $\mathrm{Re} \ll 1$. Thus, we simplify the problem by putting $\mathrm{Re} = 0$, that eliminates the only nonlinear term in the equations (6)–(7).

The flow equations must be complemented by appropriate boundary conditions. The computational domain comes from a digital image, which in our case is a subset of a rectangular box. We choose two opposite faces of this box and declare them the inlet and outlet boundaries. At these boundaries, we impose Dirichlet conditions for the pressures, zero-flow conditions for the lateral components of the flow velocities, and a zero Neumann condition for the component of velocity in the direction of the flow. Note that the fluid pressure enters the equations only through its derivatives, so it can be determined only up to a constant additive term. The Dirichlet conditions for the pressure eliminate this ambiguity in the numerical solution. The zero Neumann conditions for the velocities provide for the compatibility with Equation (7). Manwart *et al.* [27] used similar boundary conditions in a projection method of solving the Stokes equations [38].

Here, the selection of the inlet and outlet boundaries is arbitrary. Running flow simulations for different pairs of inlet–outlet faces helps to verify whether the sample is isotropic. Although the isotropy of the flow properties is not necessary for simulations, it is an assumption employed within this study.

Discretization of the differential equations

A digital image from a computer tomography scanner is a three-dimensional array of cubic voxels. **Fig. 1** shows the digital image of the pore space of a sandstone. The image resolution determines voxel size. The voxels representing the pore space naturally define a grid for discretization.

To discretize equations (6)–(7) we employ a DuFort–Frankel pattern on a staggered discretization scheme. The latter is also known as the marker-and-cell method (MAC) [39]. The DuFort–Frankel pattern is an explicit three-layer scheme. As an explicit scheme, it requires a relatively small amount of computations per time step. At the same time, it is known to be unconditionally stable for some classes of boundary-value problems [40]. Convergence and stability of this scheme for the Navier–Stokes equations have been confirmed by numerical experiments [34].

The artificial compressibility factor δ should be selected to optimize convergence and stability of the iterations. A smaller compressibility should lead faster to an incompressible flow solution, but may increase the risk of losing stability by making the system of equations stiff. A larger compressibility can slow down the convergence to a steady solution, especially for Equation (7). To selected a suitable value for δ, we have used test computations.

In a MAC discretization, the velocities are evaluated at the center points of the interfaces between the grid cells, whereas the densities and pressures are evaluated at the centers of the voxels, **Fig. 2**. Only the components of the velocities which are normal to the cell walls matter in the computations. For example, v_x is evaluated only at the centers of those voxel faces, which are orthogonal to the x coordinate axis.

Indexing convention. Let N_x, N_y, and N_z be the dimensions of the grid. We enumerate the grid cells by zero-based indices $i = 0, 1, \ldots, N_x - 1$, $j = 0, 1, \ldots, N_y - 1$, and $k = 0, 1, \ldots, N_z - 1$. Each velocity component is evaluated at the centers of two opposite walls of the voxel. For enumeration, we adopt the convention that the velocity is always associated with the upstream (with respect to the indexing) boundary. For example, **Fig. 2** shows the velocity components $v_{x,\,i,j,k}$, $v_{y,\,i,j,k}$, and $v_{z,\,i,j,k}$ associated by this indexing with the voxel (i, j, k). Let h denote the voxel edge length, and let the origin of the reference coordinate system be associated with the upstream corner of the entire image. Then the coordinates of the voxel center are $x = (i + 0.5)h$, $y = (j + 0.5)h$, and $z = (k + 0.5)h$. The x velocity component, v_x, is evaluated at the point with coordinates $(ih, (j + 0.5)h, (k + 0.5)h)$. The indexing conventions for the other velocity components are similar. **Fig. 3** shows an example of indexation of the pressures and velocities at the cross-section of the

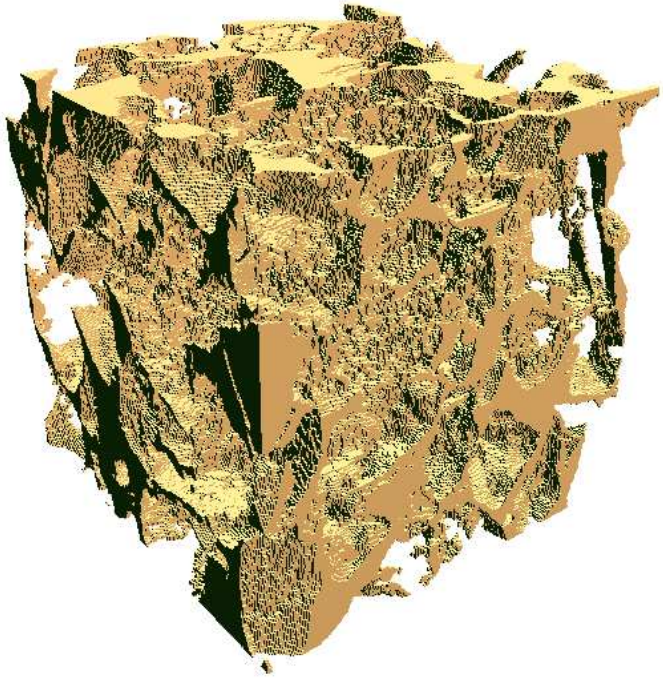

Figure 1: A 3D digital image of the pore space of sandstone, $250 \times 250 \times 250$ **voxels.**

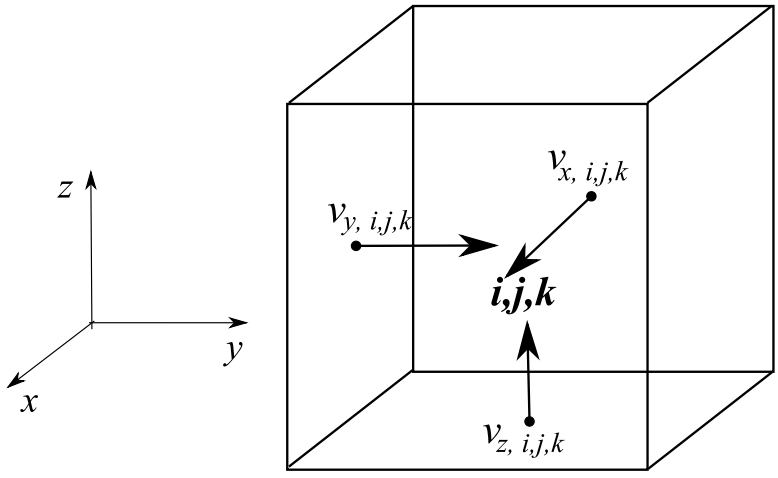

Figure 2: Voxel and fluid velocity components enumeration: $i_v = i+1$, $j_v = j+1$, **and** $k_v = k+1$, **where** i, j, k **are the indices of the voxel center.**

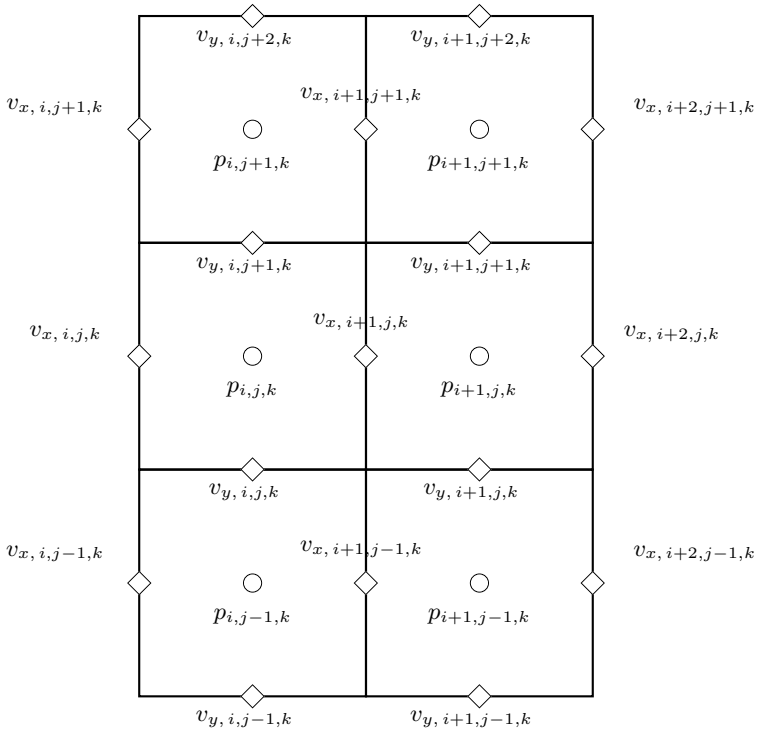

Figure 3: The circles mark the voxel centers, where the pressures are evaluated. The diamonds mark the centers of the interfaces between voxels, where the velocities are evaluated. This is a 2D slice of a 3D grid in plane x, y.

interior part of the grid by the plane orthogonal to z and passing through $z = (k + 0.5)h$. The diamond markers label the points at the voxel walls where the velocities are evaluated. The circles mark voxel centers.

The indexing described above does not cover the outer downstream boundaries of the image. To incorporate the boundary conditions and complete the finite-difference equations, the regular part of the discrete domain described above is complemented by three two-dimensional velocity arrays associated with ghost voxels.

Finite-difference equations. Let τ denote an increment step of the variable t. Note that the "time" variable t in Equations (6)–(7) is an iteration parameter, rather than a physically meaningful measure of time. A zero-based superscript index ^{n} denotes the enumeration corresponding to t. For example, $v^n_{x,\,i,j,k}$ denotes the n-th iteration of the x-component of the velocity $\mathbf{v}$ evaluated at the center of the upstream (in the direction x) wall of the voxel i, j, k. Similarly, the discretized dimensionless pressures and artificial densities are denoted, respectively, by $p^n_{i,j,k}$ and $\rho^n_{i,j,k}$.

The DuFort–Frankel pattern is a three-layer scheme. Let us describe the procedure of evaluation of the $(n + 1)$-th iteration for the velocities, artificial densities and pressures based on the $(n - 1)$-th and n-th iterations. The central difference provides a second-order approximation for the first-order derivatives. For example,

$$\left.\frac{\partial v_x}{\partial t}\right|^n_{i,j,k} = \frac{v^{n+1}_{x,\,i,j,k} - v^{n-1}_{x,\,i,j,k}}{2\tau} + O(\tau^2) \tag{9}$$

$$\left.\frac{\partial p}{\partial x}\right|^n_{i,j,k} = \frac{p^n_{i,j,k} - p^n_{i-1,j,k}}{h} + O(h^2) \tag{10}$$

Note that although the discretized pressures and velocities are evaluated, respectively, at voxel centers and voxel walls, the estimates in Equations (9) and (10) are valid at the voxel wall: $x = ih$, $y = (j + 0.5)h$, and $z = (k + 0.5)h$. In the DuFort–Frankel scheme, the

second-order partial derivatives in x, y and z are approximated in the following way:

$$\left.\frac{\partial^2 v_x}{\partial x^2}\right|_{i,j,k} \approx \frac{(v^n_{x,\,i+1,j,k} - v^{n+1}_{x,\,i,j,k}) - (v^{n-1}_{x,\,i,j,k} - v^n_{x,\,i-1,j,k})}{h^2} \tag{11}$$

$$\left.\frac{\partial^2 v_x}{\partial y^2}\right|_{i,j,k} \approx \frac{(v^n_{x,\,i,j+1,k} - v^{n+1}_{x,\,i,j,k}) - (v^{n-1}_{x,\,i,j,k} - v^n_{x,\,i,j-1,k})}{h^2} \tag{12}$$

$$\left.\frac{\partial^2 v_x}{\partial z^2}\right|_{i,j,k} \approx \frac{(v^n_{x,\,i,j,k+1} - v^{n+1}_{x,\,i,j,k}) - (v^{n-1}_{x,\,i,j,k} - v^n_{x,\,i,j,k-1})}{h^2} \tag{13}$$

Equations (9)–(13) yield the following finite-difference approximation of the x component of the creeping-flow approximation (Re $= 0$) of Equation (6):

$$\frac{v^{n+1}_{x,\,i,j,k} - v^{n-1}_{x,\,i,j,k}}{2\tau} = \frac{v^n_{x,\,i-1,j,k} + v^n_{x,\,i+1,j,k} - v^{n-1}_{x,\,i,j,k} - v^{n+1}_{x,\,i,j,k}}{h^2} + \frac{v^n_{x,\,i,j-1,k} + v^n_{x,\,i,j+1,k} - v^{n-1}_{x,\,i,j,k} - v^{n+1}_{x,\,i,j,k}}{h^2} + \frac{v^n_{x,\,i,j,k-1} + v^n_{x,\,i,j,k+1} - v^{n-1}_{x,\,i,j,k} - v^{n+1}_{x,\,i,j,k}}{h^2} + \frac{\rho^n_{i+1,j,k} - \rho^n_{i,j,k}}{\delta h} \tag{14}$$

The y and z components of the Stokes equations are approximated in a similar manner. For the artificial compressibility equation (7), one obtains:

$$\frac{\rho^{n+1}_{x,\,i,j,k} - \rho^{n-1}_{x,\,i,j,k}}{2\tau} = \frac{v^n_{x,\,i,j,k} - v^n_{x,\,i-1,j,k}}{h} + \frac{v^n_{y,\,i,j,k} - v^n_{y,\,i,j-1,k}}{h} + \frac{v^n_{z,\,i,j,k} - v^n_{z,\,i,j,k-1}}{h} \tag{15}$$

The finite-difference Equations (14)–(15) provide second-order approximations to the respective partial differential equations.

Discretization of the boundary conditions. The problem under consideration involves two types of boundary conditions. At the pore walls inside the sample image, we impose no-slip conditions. At the boundaries of the whole image, the boundary conditions are different depending on the direction of the flow. To mimic a macroscopic pressure gradient, we impose Dirichlet conditions for the pressures at the inlet and outlet faces. For the flow velocities, we impose zero Dirichlet conditions for the lateral components, and a zero Neumann condition for the component aligned with the macroscopic pressure gradient. For the velocities at the lateral boundaries of the domain, we impose zero Dirichlet conditions. This section, discusses the implementation of these boundary conditions in more detail.

Discretization of the no-slip boundary conditions at the pore walls inside the image. Incorporation of the no-slip boundary condition merely means an appropriate modification of Equations (14) when one of the nodes of the stencil occurs at a pore wall or inside the solid phase. There are several typical configurations, which are considered individually. In the two-dimensional illustrations, the solid voxels are shaded and the pore voxels are blank. A solid diamond marker labels the stencil center point for the discretized Stokes equation (14). The stencils, on which the Stokes equations are discretized, are centered at the interfaces between pore voxels. The stencil for Equation (15) are centered at the voxel centers.

Handling a situation where the velocity component is orthogonal to the pore wall is straightforward. For example, in a configuration shown in **Fig. 4**, the no-slip boundary condition, $v^n_{x,\,i,j,k} = 0$, transforms Equation (11) into

$$\left.\frac{\partial^2 v_x}{\partial x^2}\right|^n_{i,j,k} \approx \frac{v^n_{x,\,i+1,j,k} - v^{n+1}_{x,\,i,j,k} - v^{n-1}_{x,\,i,j,k}}{h^2} \tag{16}$$

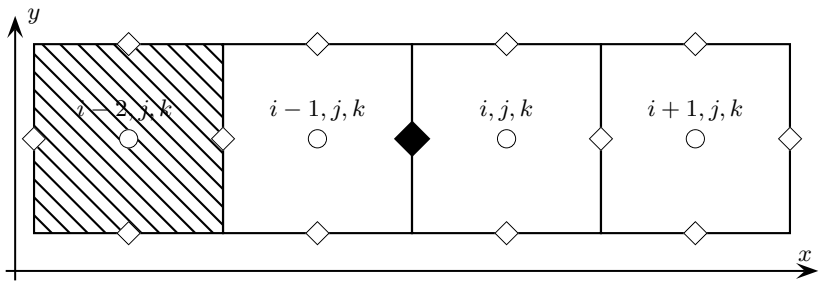

Figure 4: A stencil encountering a pore wall on the left. The filled diamond marks the center of the stencil.

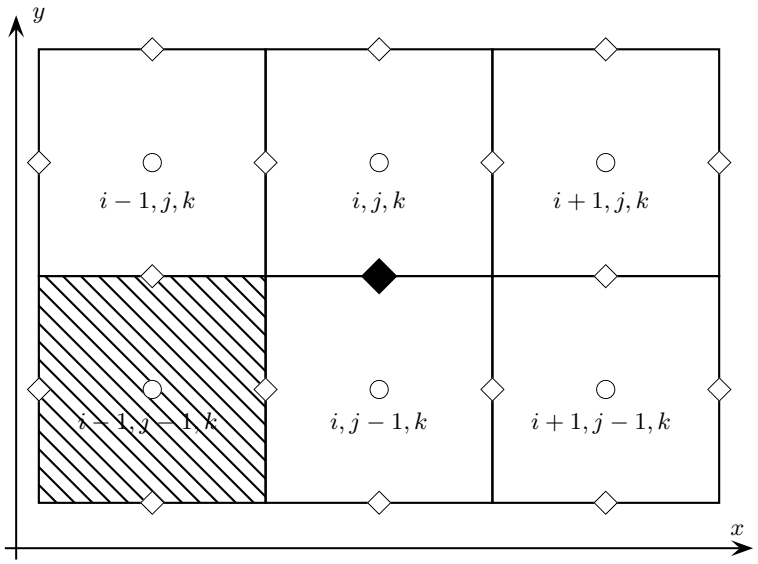

Figure 5: A stencil with a pore wall corner.

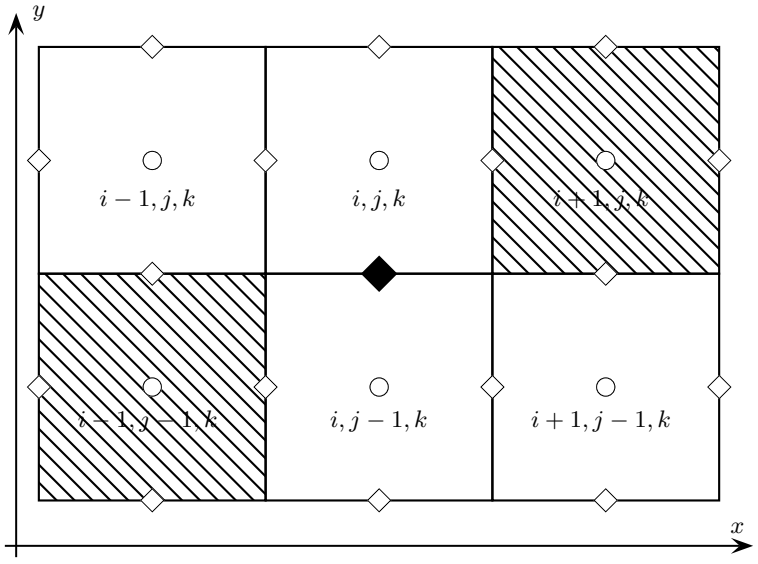

Figure 6: A stencil with two pore wall corners.

To show how to incorporate the no-slip boundary conditions into discretization of the second partial derivative of a velocity component in an orthogonal direction, consider $\dfrac{\partial^2 v_y}{\partial x^2}$. In a configuration like in **Fig. 5**, for an arbitrary n the no-slip condition implies $v^n_{y,\,i-1,j,k} = 0$. Hence, in such a configuration, we put

$$\left.\frac{\partial^2 v_y}{\partial x^2}\right|^n_{i,j,k} \approx \frac{v^n_{y,\,i+1,j,k} - v^{n-1}_{y,\,i,j,k} - v^{n+1}_{y,\,i,j,k}}{h^2} \tag{17}$$

In a situation shown in **Fig. 6**, one obtains

$$\left.\frac{\partial^2 v_y}{\partial x^2}\right|^n_{i,j,k} \approx \frac{-v^{n-1}_{y,\,i,j,k} - v^{n+1}_{y,\,i,j,k}}{h^2} \tag{18}$$

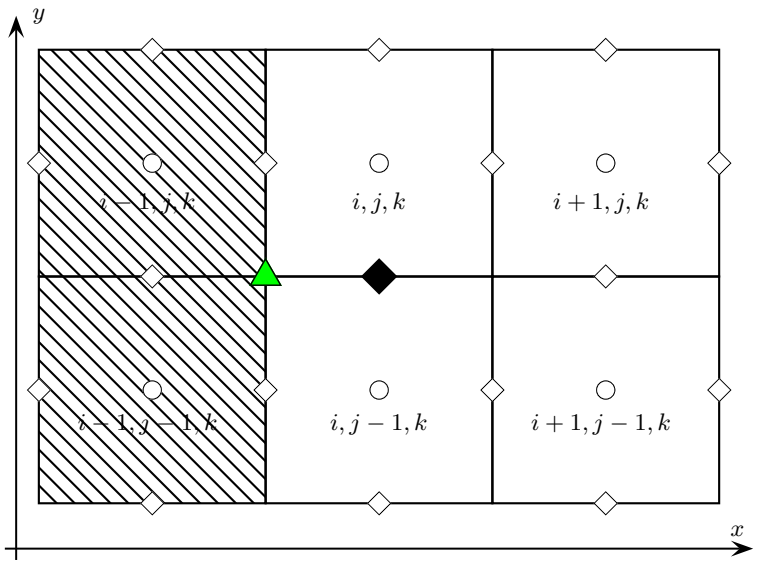

Figure 7: A stencil encountering a pore wall. The center of the stencil is labelled by a filled diamond, whereas the triangle marks the boundary between the solid wall and pore space.

If the stencil encounters a wall, as in **Fig. 7**, then the no-slip boundary condition must be formulated at the midpoint marked by the triangle. The interface between the voxels $i-1,j,k$ and $i-1,j-1,k$ is inside the solid phase, so we use the center of this interface as a ghost node where v_y is equal to $-v^n_{y\,i,j,k}$. Thus, the approximation of the second derivative of v_y with respect to x takes on the form:

$$\left.\frac{\partial^2 v_y}{\partial x^2}\right|^n_{i,j,k} \approx \frac{v^n_{y,\,i+1,j,k} - v^n_{y,\,i,j,k} - v^{n+1}_{y,\,i,j,k} - v^{n-1}_{y,\,i,j,k}}{h^2} \tag{19}$$

Boundary conditions at the boundaries of the entire sample. To formulate the boundary conditions for the entire image of the sample, it is wrapped with a single layer of pore voxels. The boundary conditions are formulated at the planes passing through the centers of these wrapping voxels. The boundary nodes are shown as filled circles and filled diamonds in **Fig. 8**.

To impose Dirichlet boundary conditions for the pressures and artifitial densities at the inlet and outlet, we merely assign their values at the respective voxel centers. For example, let the flow be in the x direction. At all boundary nodes i,j,k with either $i = 0$ or $i = N_x - 1$ we assign the pressures to mimic the pressure gradient $(1,0,0)$. For example:

$$\rho_{i,j,k} = 1 + \frac{\delta h(N_x - 1 - i)}{N_x - 1} \tag{20}$$

In fact, one can use the formula in Equation (20) as the initial condition for the densities over the entire pore space.

To formulate the boundary conditions for velocities, we add to the grid a single layer of ghost voxels at the downstream boundary in each direction. For example, in x direction, next to the boundary voxels $N_x - 1, j, k$, we define a double array of ghost velocity components $v^{\text{ghost}}_{x,\,j,k}$. The ghost arrays $v^{\text{ghost}}_{y,\,i,k}$ and $v^{\text{ghost}}_{z,\,i,j}$ are introduced in a similar manner.

Since velocity components are evaluated at the centers of the voxels faces, discretization of the zero-flow Dirichlet condition is straightforward. For the component v_x, the central difference provides a second-order approximation of the normal derivative. That is, for example, for a zero Neumann boundary condition at the inlet voxels we put

$$v_{x,\,0,j,k} = v_{x,\,1,j,k} \tag{21}$$

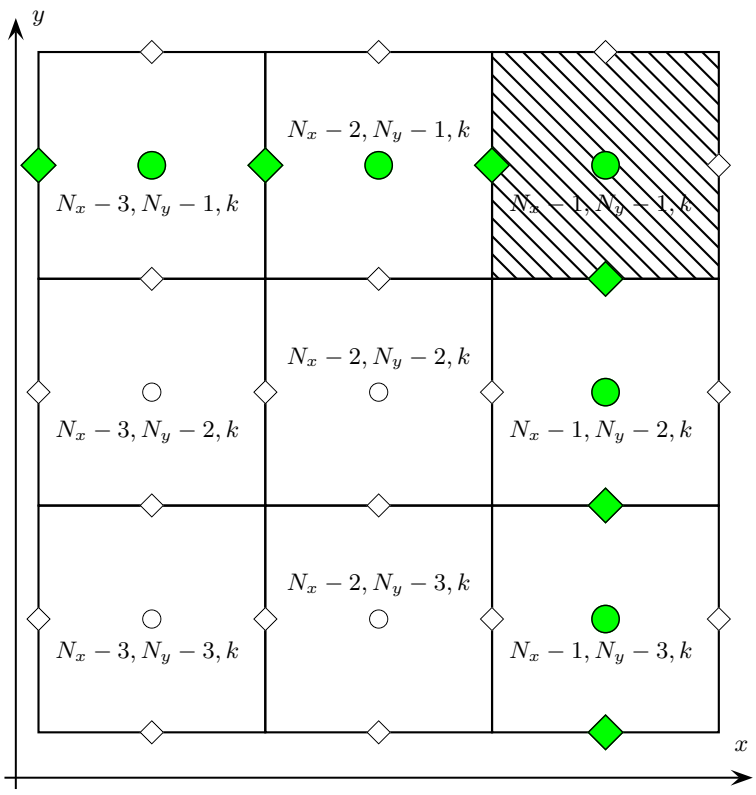

Figure 8: Discretization of the boundary conditions at the boundary of entire sample: filled circles and diamonds denote boundary nodes. The shaded corner voxel does not enter the discretized boundary conditions.

for all j, k.

On each lateral boundary of the sample, two velocity components are evaluated at the boundary. For these components, discretization of the Dirichlet condition is straightforward. For the third component, a linear interpolation provides a second-order approximation. For example, for v_y on the top boundary in **Fig. 8**, one gets

$$v_{y,\,i,N_y-1,k} + v^{\text{ghost}}_{y,\,i,k} = 0 \tag{22}$$

where $v^{\text{ghost}}_{y,\,i,k}$ is the ghost velocity component defined above.

Note that the discretization described above does not involve the velocity components evaluated at the external boundaries of the vertex and edge voxels of the image. The values of the artificial density ρ at the corner nodes of the domain are not involved as well.

Computational parameters. To choose values for the artificial compressibility, an iteration step τ, and a stopping criterion, the algorithm has been applied to two problems admitting analytical solutions: Poiseuille flow in a pipe of square cross-section, and the Stokes problem of laminar creeping flow around a solid sphere. We have chosen 10 voxel sizes as the dimensionless length unit, so that $h = 0.1$. For each velocity component and the artificial density, the mean square relative increment was the measure of the increment at each iteration. For example, for the x component of velocity, v_x, we evaluate

$$DV^n_x = \frac{\sum\limits_{i,j,k} \left| v^{n+1}_{x,\,i,j,k} - v^n_{x,\,i,j,k} \right|^2}{\sum\limits_{i,j,k} \left(v^n_{x,\,i,j,k} \right)^2} \tag{23}$$

The iteration continue until fulfilling the stopping criterion

$$\max \left\{ DV^n_x, DV^n_y, DV^n_z, D\rho^n, \right\} \le \varepsilon_{\text{tol}} \tag{24}$$

The numerical computations for the Poiseuille flow showed stability and fast convergence of the algorithm for a wide range of artificial compressibility values. **Fig. 9** shows plots of exact and numerical profiles of velocity component $v_x = v_x(y)$ for the flow in x direction for various cross-sections by planes orthogonal to the z axis.

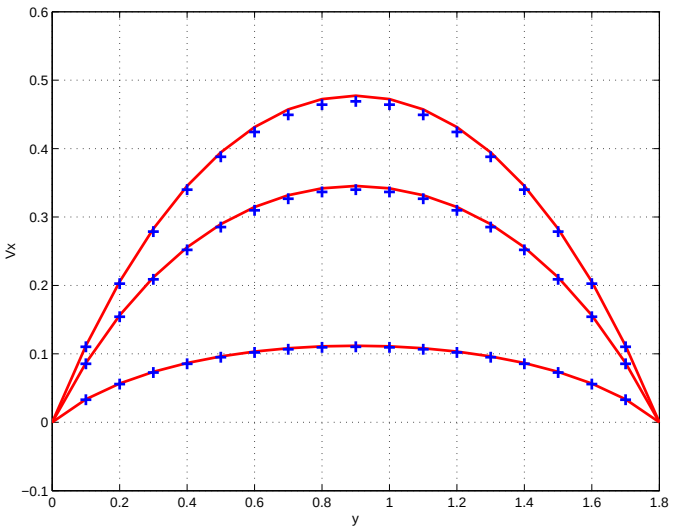

Figure 9: Comparison of computed (crosses) and exact solutions (solid lines) for Poiseuille flow. The stopping criterion ε_{tol} was set equal to 10^{-8}.

The good convergence for the Poiseuille flow example should not be surprising. Although the computations are performed on a three-dimensional domain, the velocity component v_x remains independent of z in all iterations, and the other two components remain identically equal to zero. Thus, the inlet and outlet boundary conditions are satisfied automatically and the dimensionality of the problem reduces to 2. Moreover, the vanishing velocity and pressure gradient components reduce the problem to a single two-dimensional Dirichlet boundary-value problem for a Poisson equation. In such a case, the stability and convergence of the DuFort–Frankel scheme has been demonstrated theoretically [40]. An additional testing of the algorithm on the Stokes problem of laminar creeping flow around a solid sphere of radius R in an infinite domain has shown that, actually, the convergence and stability of the algorithm are both sensitive to the choice of the time step τ. We have found that values near $\tau = 10^{-3}$ were suitable both for the Poiseuille and Stokes problems.

On the surface of the sphere, the velocity satisfy no-slip boundary conditions, and it is equal to $\mathbf{v}_\infty$ at infinity. The exact creeping-flow solution is given by equation

$$\mathbf{v}(\mathbf{r}) = \mathbf{v}_\infty - \frac{3R}{4r}\left(\mathbf{v}_\infty + \mathbf{n}(\mathbf{v}_\infty \cdot \mathbf{n})\right) - \frac{R^3}{4r^3}\left(\mathbf{v}_\infty - 3\mathbf{n}(\mathbf{v}_\infty \cdot \mathbf{n})\right) \tag{25}$$

see [37]. Here $\mathbf{r}$ is the radius-vector from the center of the sphere, and r is the distance from the center: $r = \|\mathbf{r}\|$. For the dimensionless pressure, one has

$$p(\mathbf{r}) = p_\infty - \frac{3R}{2r^2}\,\mathbf{u}_\infty \cdot \mathbf{n} \tag{26}$$

where p_∞ is the fluid pressure at infinity. Note that in this example the normal derivative of the pressure is non-zero at the boundary. It means that the zero Neumann condition for pressures in [27] is invalid in a complex-geometry pore space.

To evaluate numerically the flow near a sphere of the radius of 5 voxel widths, we embed the sphere in a $25 \times 25 \times 25$ voxel surrounding grid. At all outer boundaries of the entire domain, we impose Dirichlet boundary conditions for the velocities using the trace of the exact solution (25).

Fig. 10 shows a cross-section of the numerically-evaluated vector field. **Fig. 11** shows three profiles of the x component of the velocity, v_x, plotted versus y for three different x. The bottom profile corresponds to the line A in **Fig. 10**. The top profile is near the outlet boundary (line C), and the one in the middle is at a midpoint between the sphere surface and the boundary, line B. Both the analytical and numerical solutions are evaluated at the voxel centers. The velocities obtained numerically are projected on the voxel centers by taking the arithmetic mean of the values at the opposite faces for each component. The reason why neither the exact solution nor the numerical one attain zero at the sphere surface is discretization: none of the voxel centers occurs exactly on the surface of the sphere. **Fig. 12** shows a similar comparison for the pressure profiles.

Even though the resemblance between the discretized sphere and an ideal spherical body is very approximate, see **Fig. 14**, the comparison between the numerical and exact solutions is encouraging. One has to observe that this accuracy has been achieved by applying a rather stringent stopping criterion: $\varepsilon_{\text{tol}} = 10^{-8}$. Attempts of relaxation of this criterion negatively affected the accuracy of the numerical solution, **Fig. 13**. At the same time, attempts of further enhancement of the tolerance in the stopping criterion, $\varepsilon_{\text{tol}} = 7.5 \times 10^{-10}$, resulted in no appreciable improvement of the accuracy.

The Darcy velocity is evaluated as the mean value of the fluid velocity over the entire grid. **Fig. 16** shows that the estimate of the component of the Darcy velocity in the downstream direction stabilizes after a sufficiently large number of iterations. The relative increments also stabilize near a value between 10^{-9} and 10^{-8}, **Fig. 17**.

A refinement of the discretization by dividing the voxel size by two has not significantly improved the accuracy of the numerical solution. The plots in **Fig. 15** compare the velocity profiles evaluated numerically for two grids and the exact solution.

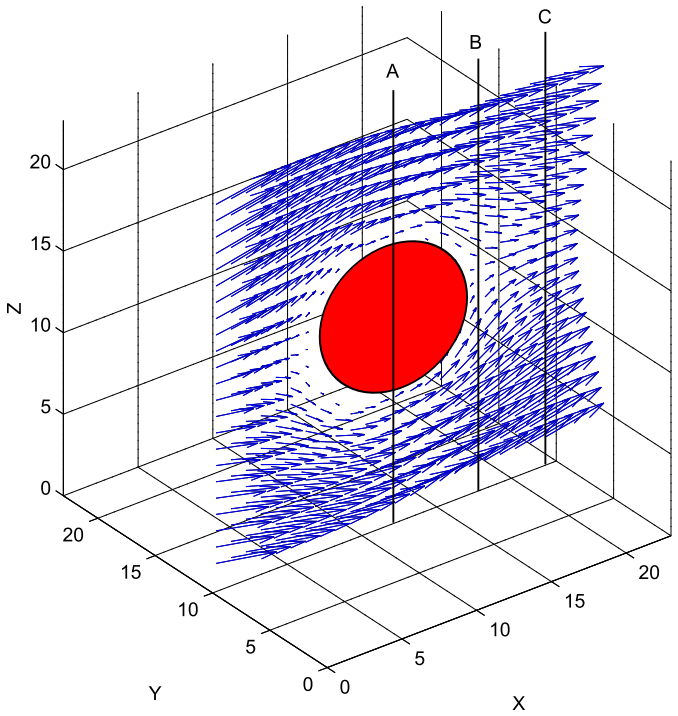

Figure 10: A central cross-section of the velocity field evaluated numerically.

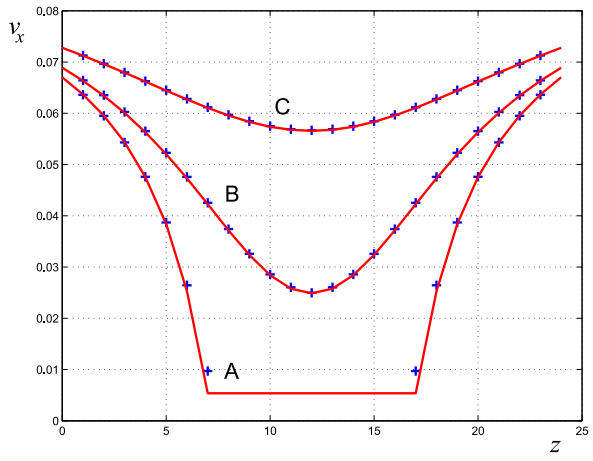

Figure 11: Three velocity profiles corresponding to cross-sections A, B and C, Fig. 10: a comparison between exact solution (Eq. (25)) and numerical solution in dimensionless units. The solid lines show the exact solutions and the crosses show the numerical ones.

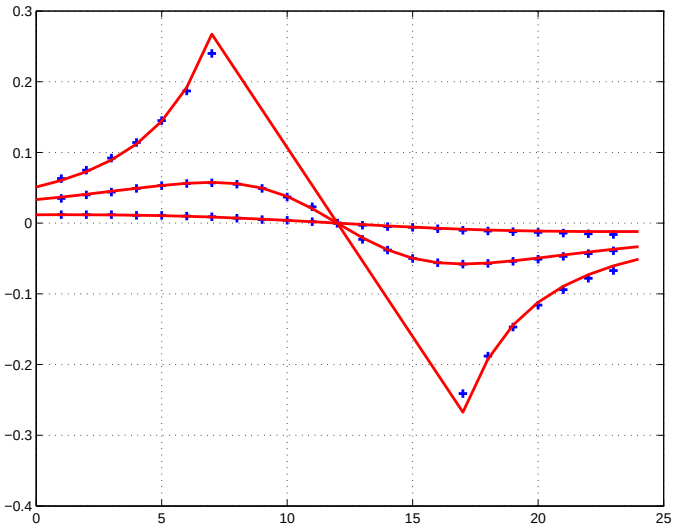

Figure 12: Three pressure profiles: a comparison between exact solution (Eq. (25)), shown as a solid line, and numerical solution, crosses, in dimensionless units.

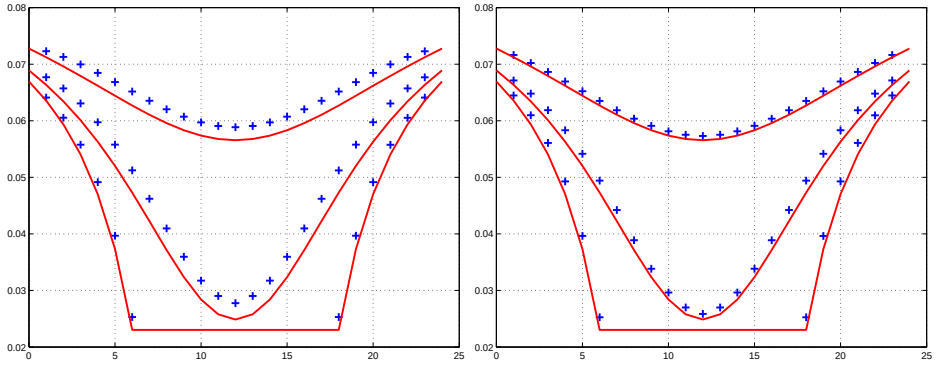

Figure 13: Velocity profiles shown in Fig. 11 for relaxed stopping criterion: $\varepsilon_{tol} = 7.5 \times 10^{-7}$ on the left, and $\varepsilon_{tol} = 7.5 \times 10^{-8}$ on the right.

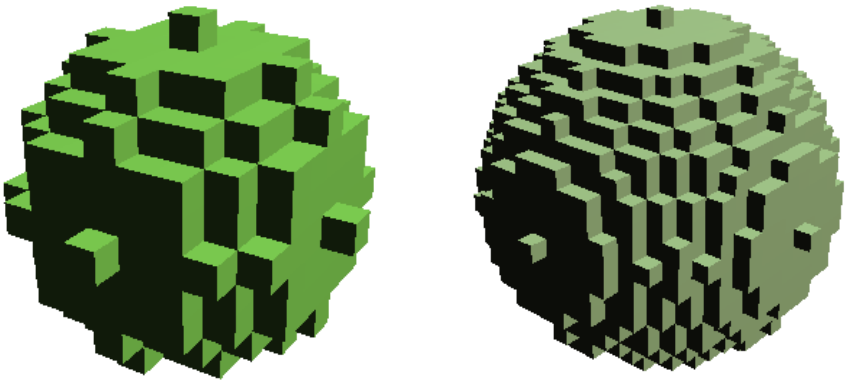

Figure 14: Discretized spheres of the radius of 5 voxel (on the left) and 10 (on the right) voxel units.

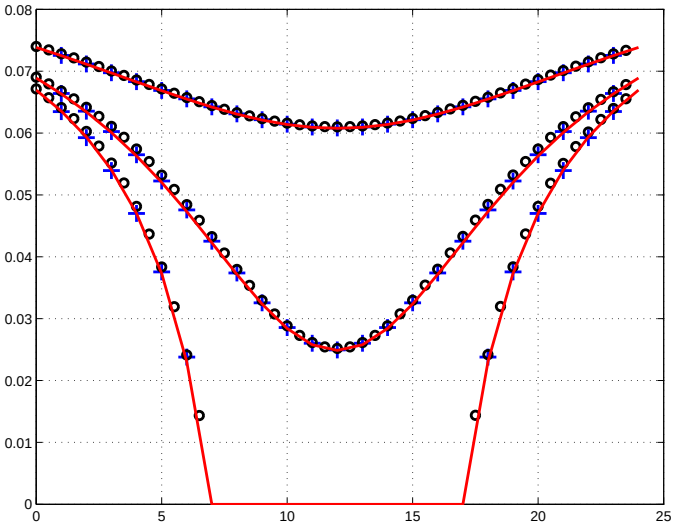

Figure 15: Velocity profiles evaluated numerically on coarse (crosses) and fine (circles) grids of voxels along with exact solution (solid line).

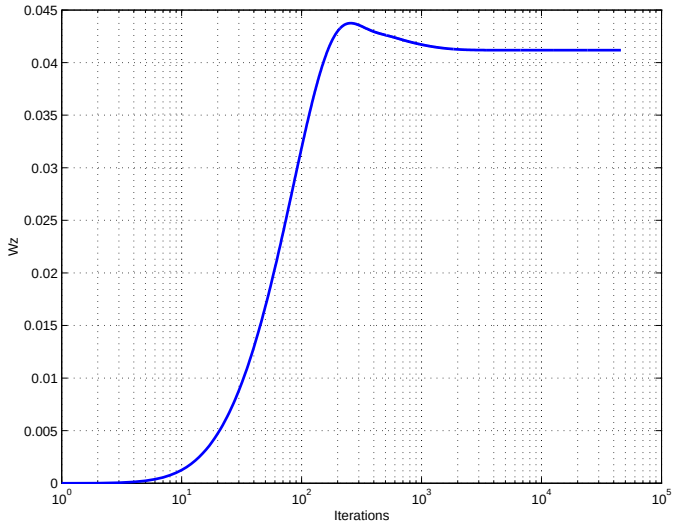

Figure 16: Stabilization of Darcy velocity estimate.

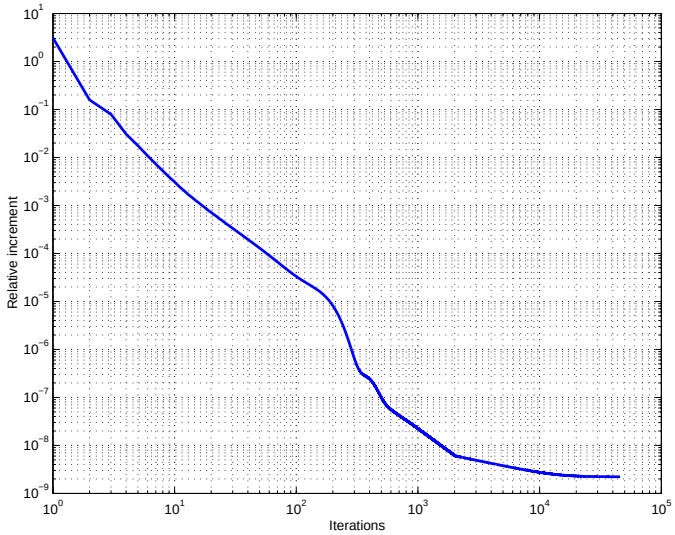

Figure 17: Stabilization of relative improvement near 10^{-9}.

Our tests of the algorithms lead to two main conclusions. First, a reasonable accuracy of the numerical computations requires a stringent stopping criterion. Second, the computations on a refined grid show that for the overall accuracy of the solution the convergence is more important than how fine the discretization is.

Partitioning the image into layers. To estimate the permeability of a sample, we solve the Stokes equations on the pore space. Averaging the velocity field leads to an estimate of the Darcy velocity. The Dirichlet boundary conditions for the pressures at the inlet and outlet of the sample provide an estimate of the macroscopic pressure gradient. Finally, from the Darcy velocity and pressure gradient, one obtains an estimate of the permeability. We assume that the flow properties of the sample are isotropic. A repetition of the flow simulations in the three coordinate directions, that is for three different choices of the inlet and outlet boundaries, reduces the uncertainty of the estimates.

Meeting the severe convergence requirements discussed above can be computationally demanding. It was impossible to attain the tolerance criterion on a large domain within a reasonable number of iterations. To reduce the dimensions of the computational domain, it is beneficial to split the entire sample into parts. Here we employ partitioning of the sample into layers, so that the lateral dimensions of each part significantly exceed the thickness. The simulations can be carried out on each part separately, and the the results can be combined by taking the harmonic mean of the permeability estimates for the individual layers.

The computations within this study have been carried out on layers with the aspect ratios between the lateral dimensions and the thicknesses between 6 and 10. On each slice, the pressure boundary conditions are imposed on the larger faces of the sample, **Fig. 18**. The permeability is evaluated three times by simulating flow in the three coordinate directions x, y, and z. To reduce the uncertainty, the average permeability estimate is used as the final output. A more thorough analysis of the limiting admissible values of the aspect ratio, sample size, the number of layers, *etc.*would be a worthwhile task, but it is beyond the scope of this work.

The no-flow lateral boundary conditions can block the flow paths which may leave or enter the sample. For example, if a rectangular sample is selected as in **Fig. 19**, then flow simulations will show zero flow along the flow paths A, C, and D. If the image is sliced in the direction of the flow, the conductances of these flow paths will be non-zero at least for some slices. At the same time, the conductance of a flow path of very complex geometry, like the one labelled by B, will be likely overestimated in the shadowed slice. **Fig. 19** is a cartoon illustration and cannot cover the full complexity of the 3D pore space geometry. It indicates that the partitioning of the entire sample image into slices may result in an overestimate of the absolute permeability if, for example, the layer crosses some flow path more than once. At the same time, the layers with large lateral dimensions reduce the impact of the no flow condition at the lateral boundaries. There is an uncertainty whether these two effects can compensate for each another.

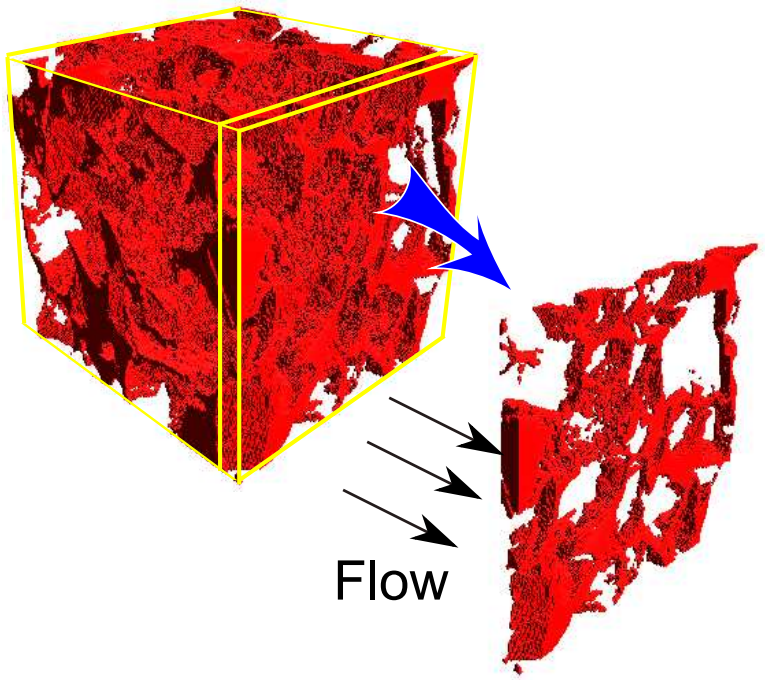

Figure 18: Partitioning of the image of the pore space into layers and solving flow equations for the flow orthogonal to the layer.

Relative permeability curves. Two- or three-phase flows of immiscible fluids are described by the generalized Darcy's law. Based on the experiments by Wyckoff and Botset [41], the foundations of the theory of multi-phase flows in porous media were developed by Muskat and Meres [42] and Leverett [43].

Consider, for example, the simultaneous flow of water and oil. Since each fluid occupies only a part of the pore space, the perme-

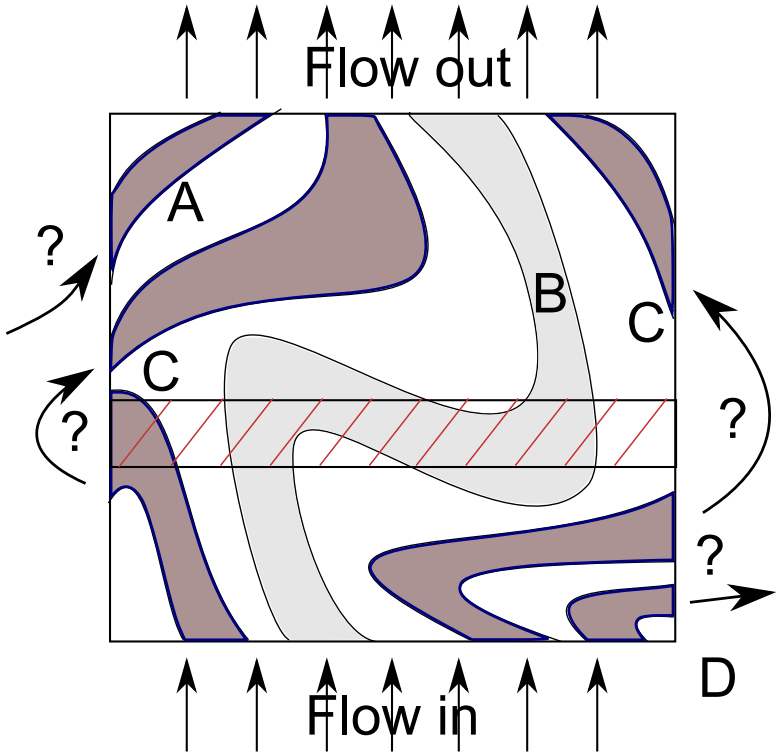

Figure 19: Uncertainties associated with modeling of the flow: Only path B is not blocked by the no-flow boundary condition. Some flow paths contributing to the overall permeability may enter through a lateral boundary A, leave and return C, and just leave D. Partitioning of the image may lead to an overestimate of conductivity of channel B in some layers.

ability to this fluid is different from the absolute permeability of the rock. A dimensionless relative permeability is a correction factor, so that the Darcy's law for each fluid has the form:

$$u_o = -\frac{k_o k}{\mu}\nabla p_o, \qquad u_w = -\frac{k_w k}{\mu}\nabla p_w \tag{27}$$

The relative volume of the pore space occupied by each fluid is its saturation. According to the classical theory, both relative permeability factors, k_o and k_w, are functions of the fluid saturations, S_o and S_w. Since the sum of both saturations is identically equal to one, the water saturation, S_w, completely characterizes the volumetric fluid distribution. Thus, one can write

$$k_o = k_o(S), \qquad k_w = k_w(S) \tag{28}$$

where $S = S_w$.

One of the main assumptions of the classical theory of multi-phase flow in porous media is in local equilibrium of the fluid distribution enforced by the capillary pressure. In general, the picture is more complex, and the flow rate and the history of fluid displacement [10, 16] can have a significant impact on the geometry of the fluid-fluid interfaces.

In this work, we assume that local equilibrium is entirely defined by the capillary pressure. In such a case, the distribution of the fluids in the pore space can be estimated using the method of maximal inscribed spheres (MIS). Briefly, the idea of the method is in assigning to each voxel the radius of the maximal sphere included in the pore space and covering this voxel. Once a three-dimensional table of such maximal radii is generated, one can simulate various invasion scenarios using cluster search algorithms. A more detailed description of the method is in [30, 31].

MIS method, in particular, involves evaluation of the fluid distribution at a given capillary pressure. With a proper scaling, it produces a reasonable approximation of the capillary pressure curve [35]. The calculated fluid distribution yields a list of the voxel which are deemed to be occupied by water or oil. The voxels occupied by one fluid can be considered as a stand-alone pore space. Thus, the permeability of this system of voxels scaled by the absolute permeability of the entire pore space is an approximation to the relative permeability factor. Counting the relative number of these voxels provides an estimate of the saturation.

To summarize, the following procedure has been employed to evaluate the relative permeability curves numerically.

1. Estimate the absolute permeability of the pore space:
   - Run flow simulations in three directions;
   - In each direction, partition the image into slices, estimate the permeability of each slice and take the harmonic mean;

- Take the average estimate for all three directions as the final output

2. Calculate fluid distribution using MIS algorithm and evaluate the respective saturations:
   - Evaluate the maximal inscribed radii;
   - The total number of radii can be large, so choose a reasonable number for the flow simulations;
   - For each chosen radius, compute the fluid distribution and saturation
3. Evaluate relative permeabilities
   - For each saturation chosen in the previous item, evaluate the permeability to each fluid;
   - Evaluate the relative permeability by taking the ratio of the estimates of the permeabilities to each fluid to the estimate of the absolute permeability;
   - Plot the relative permeabilities curves as functions of the saturation.

Fig. 20 shows the numerical results for CT images of a sandstone, and a number of experimental points obtained in coreflood laboratory experiments. A comparison can be only qualitative, since the images of the rock pore space have been acquired from similar, but not the same samples. One can see that the computed relative permeability curves, shown as solid curves with various markers on the plots, are in the same range as the experimental points. The variability of the computed relative permeabilities is similar to that of the data. Note that the scatter of the relative permeability estimated for the non-wetting fluid is larger than that for the wetting fluid. Network-based estimates by Fatt [3] showed a similar picture. The greater likelihood of the non-wetting fluid losing the connectivity can partially explain this observation. In the simulations, we used the same digital data as in [31]. Most curves have been obtained using layers whose lateral dimensions are significantly larger than the thicknesses. The range of thicknesses was between 8 and 20 voxels. The images have a significant variability of the porosity [31]. Nevertheless, the permeability curves for the wetting fluid are aligned near the average curve. This indicates that the characteristic pore space geometry is a more important factor for the relative permeability estimates than the porosity.

Fig. 21 shows plots of the computed relative permeability curves for Finney pack [44]. All plotted data points have been obtained from flow simulations on one and the same domain of dimensions $160 \times 160 \times 160$ voxels. The different curves correspond to the different partitions of the image into layers of the thicknesses of 8, 10, 12, and 16 voxels. The pair of solid thick curves is the arithmetic mean of all four results. The results are consistent, especially for the estimates of the relative permeability to the wetting fluid. However, the variability increases significantly for simulations on thicker layers. This variability mostly affects the estimates of the relative permeability to the non-wetting fluid, and is concentrated in the range of the "transient" saturations: between 40 and 75 percent. A refinement of the image resolution and more advanced computational algorithms for solving the Stokes equations apparently should extend the range of consistency of the computational results.

The fact that all simulations have been performed with no-slip boundary conditions may also introduce an uncertainty. Such an approach excludes flow coupling [45]. Water is the wetting fluid. Therefore, the water-solid contact is rough and the length scale of this roughness is beyond the resolution of the image. This roughness may require more elaborate boundary conditions based on an asymptotic analysis. At the same time, the interfacial tension makes the water-oil interface smooth, which cannot be captured by a digital image, where the boundaries are jagged unless they are aligned with the coordinate directions. At the fluid-fluid interface, such an artificial roughness of the surface may skew the momentum balance [46]. The surface roughness impacts the effective contact angle [47]. The volume of the wetting fluid occupying small pores and crevices, which is not captured due to the limited image resolution, is unknown. Therefore, the Maximal Inscribed Spheres estimates of saturation need a correction to account for this effect. In pore-network models, such a correction is usually done by assuming microporosity. **Fig. 22** compares the relative permeability curves from **Fig. 20** with a correction for a 10% microporosity saturation. A further study can lead to a better understanding of relative contribution of the roughness and discretization effects. The computed relative permeability curves for the wetting fluid better match the data from the original two-phase flow experiments by Wyckoff and Botset [41]. The computed relative permeability curves for the non-wetting fluid underestimate the experimental results, especially for the high water saturations. Besides the fact that the computed and experimental curves are for different rocks, this observation may also indicate a better connectivity of the nonwetting fluid in the experiment. The absolute permeability of the sand packs used in the experiments was between 17.8 and 262 Darcy [41], which is much higher than that of a typical sandstone.

Summary and conclusions

Solving the incompressible creeping flow equations by a finite-difference method is a feasible approach to estimating flow properties of a porous medium from a three-dimensional computer tomography image of the pore space. In this work, we have studied a finite-difference solution of the Stokes' equations based on the method of artificial compressibility. The pore voxels of the digital image provide a natural mesh for discretizing the differential equations and boundary conditions. A three-layer Dufort–Frankel scheme on marker-and-cell staggered grid has been used in the numerical simulations. The computational parameters, including the coefficient of artificial compressibility, the magnitude of iteration step, and the stopping criterion, have been selected by trial and error. The criterion for stopping the iterations has been formulated in terms of the relative increment of the quadratic norm of the numerical solution. Numerical evaluation of the known analytical solutions, Poiseuille flow in a pipe of a rectangular cross-section and Stokes flow around

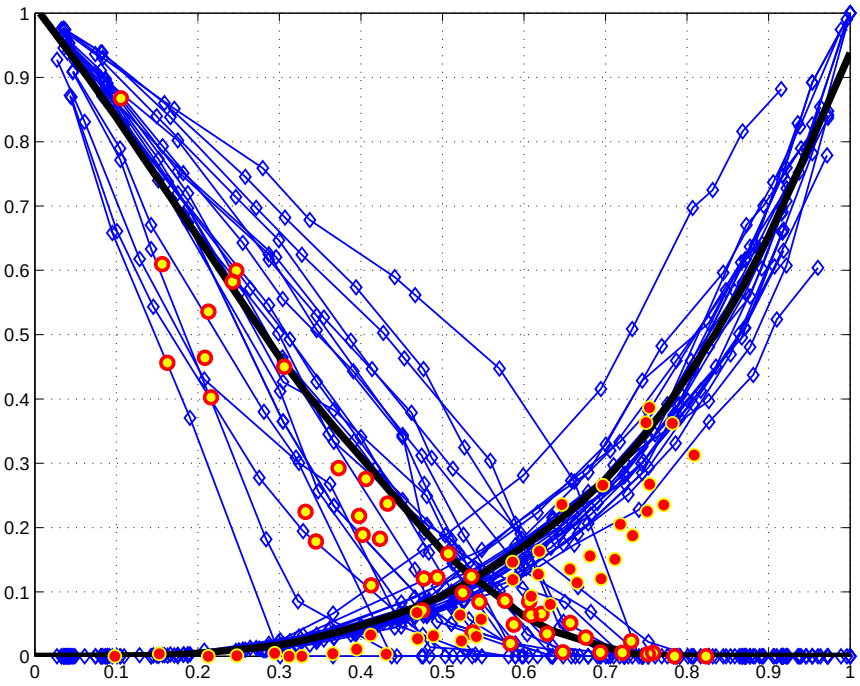

Figure 20: Computed relative permeability curves (solid lines with markers) and laboratory data (circles). The thick solid curves are average relative permeabilities. The coreflood data are courtesy of Statoil.

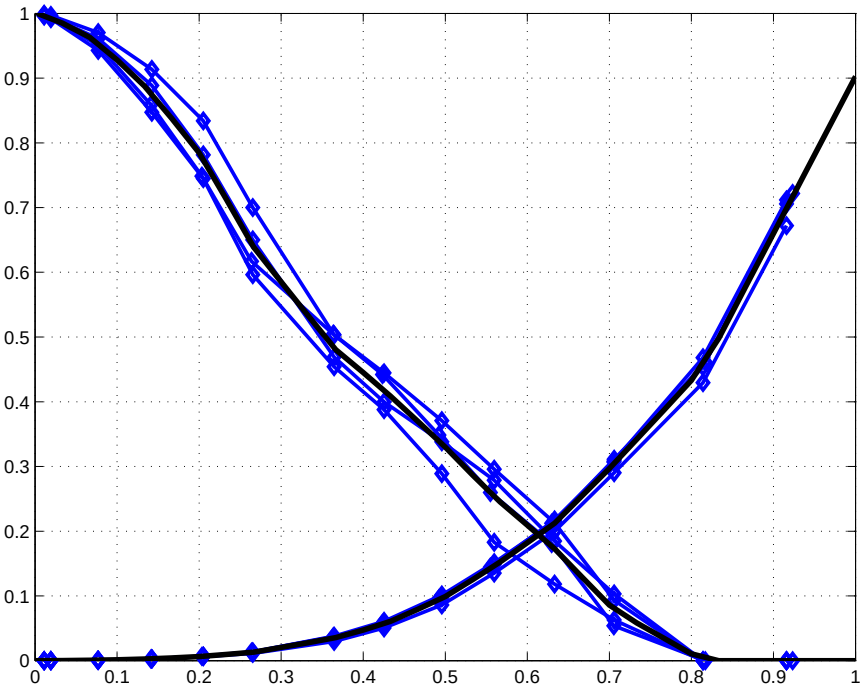

Figure 21: Computed relative permeability curves for Finney pack [44]. Different curves correspond to four different thicknesses of the partitioning layers, Fig. 18. The thick solid curves are the averages of these curves.

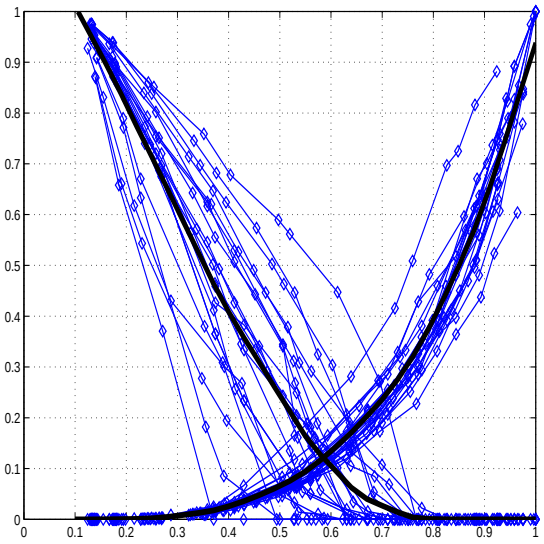

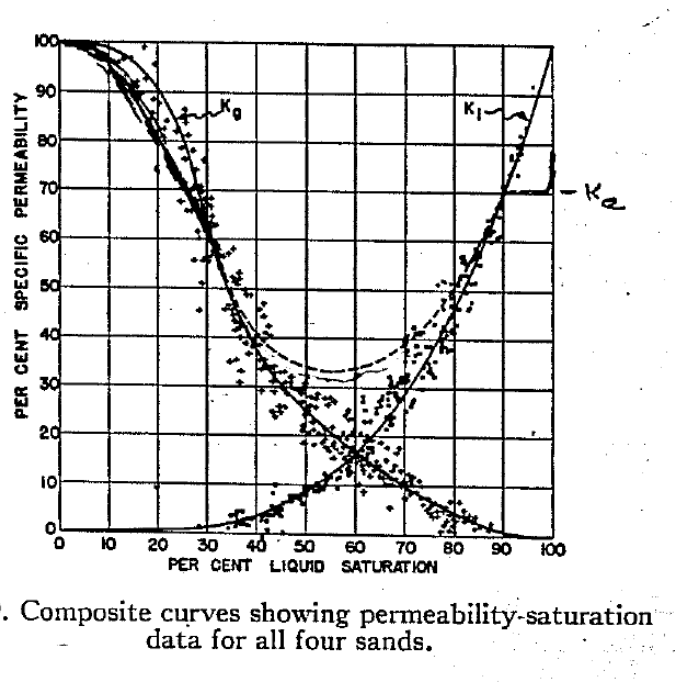

FIG. 9. Composite curves showing permeability-saturation data for all four sands.

Figure 22: Computed relative permeability curves on the left-hand plot, corrected for a 10 % microporosity saturation, resemble the experimental relative permeability curves from the original paper by Wyckoff and Botset [41].

a solid sphere, have demonstrated that the stopping criterion significantly affects the accuracy of the results. In fact, it turns out that a severe criterion is required to achieve convergence suitable for a dependable estimation of the permeability.

To reduce the computational intensity, the entire image of the porous sample is partitioned into layers. Prior to numerical simulations, the clusters of voxels, which are not connected to the inlet and outlet faces, are eliminated to reduce the size of the computational domain. Although this operation does not dramatically reduce the dimensions of the grid, it eliminates isolated stagnant-flow domains. The harmonic mean of the coefficients of permeability computed for the individual layers provides an estimate of the permeability of the entire sample. This approach makes possible to reduce the boundary effects introduced by the no-flow conditions at the lateral walls. At the same time, the partitioning into layers may lead to an overestimate of the permeability by, for example, accounting for some flow channels multiple times. Evaluation of the permeability of a porous material from a small sample is always subject to a high degree of uncertainty. For an isotropic medium, averaging the results of flow simulations in three different coordinate directions can reduce this uncertainty.

The method of Maximal Inscribed Spheres calculates the capillarity-dominated fluid distribution in the pore space of a water-wet rock. This distribution has been used to evaluate the sample permeability to each fluid at a given saturation. The relative permeability is defined as the dimensionless ratio of the phase permeability to the absolute permeability of the medium. The permeability to each phase at a given saturation has been estimated using the same algorithm as for the evaluation of the absolute permeability. Computations performed on 3D micron-scale resolution images of a sandstone produced relative permeability curves qualitatively reproducing the experimental data. This conclusion is based on the comparison of the computed curves with the original relative permeability measurements by Wyckoff and Botset for high-permeability sand packs [41]. The layer-partitioning technique may produce a significant error when applied to tight rocks, where the connectivity of the nonwetting phase may require high capillary pressure. In such case, a different technique of permeability computation may be needed. Such a technique will be considered elsewhere.

The approach discussed here is a promising tool for analysis of the petrophysical properties of natural rocks and other types of porous media. A direct analysis of an image of the pore space bypasses the challenges of network extraction unavoidable in the pore-network analysis. The proposed method can be applied to evaluate the impact of pore space geometry modifications on the rock flow properties. Such modifications can come from mechanical or thermal deformations, damage, formation or dissociation of hydrates, mineral deposition or dissolution. Exact numbers are subject to great uncertainty, both in numerical and laboratory experiments. Numerical simulations can generate trends and, therefore, provide useful insights for optimization of hydrocarbon recovery technologies, or efficient environmental remediation. The robustness of the algorithms used in this study makes the method suitable for routine applications, requiring minimum human interference. The current trends in the price of the computing and data storage resources makes the proposed approach even more attractive.

Acknowledgements

This work has been performed at Lawrence Berkeley National Laboratory (LBNL) of the U.S. Department of Energy under Contract No. DE-AC03-76SF00098 and University of California, Berkeley. The first author acknowledges support from the UC Oil Consortium

and from the U.S. Department of Energy's Assistant Secretary for Coal through the Zero Emission Research and Technology Program under the U.S. Department of Energy contract no. DE-AC02-05CH11231 to LBNL.

The authors are thankful to Dr. Andrea Cortis and Dr. Jonathan Ajo-Franklin of the Earth Sciences Division for reviewing the manuscript and useful suggestions.

References

[1] Fatt, I.: "The network model of porous media. 1. Capillary pressure characteristics," *Trans. AIME* (1956) **207**, No. 7, 144–159.
[2] Fatt, I.: "The network model of porous media. 2. Dynamic properties of a single size tube network," *Trans. AIME* (1956) **207**, No. 7, 160–163.
[3] Fatt, I.: "The network model of porous media. 3. Dynamic propertries of networks with tube radius distribution," *Trans. AIME* (1956) **207**, No. 7, 164–181.
[4] Bakke, S. and Øren, P. E.: "3-D pore-scale modeling of sandstones and flow simulations in the pore networks," *SPE Journal* (1997) **2**, 136–149.
[5] Øren, P. E., Bakke, S., and Arntzen, O. J.: "Extending predictive capabilities to network models," *SPE Journal* (1998) No. December, 324–336.
[6] Blunt, M. J. and King, P.: "Relative permeabilities from two- and three-dimensional pore-scale metwork modeling," *Transport in Porous Media* (1991) **6**, 407–433.
[7] Bryant, S. and Blunt, M.: "Prediction of Relative Permeability in Simple Porous-Media," *Physical Review A* (1992) **46**, 2004–2011.
[8] Bryant, S. L., King, P. R., and Mellor, D. W.: "Network Model Evaluation of Permeability and Spatial Correlation in a Real Random Sphere Packing," *Transport in Porous Media 11: 53-70, 1993.* (1993) **11**, 53–70.
[9] Blunt, M. J. and Sher, H.: "Pore Network Modeling of Wetting," *Physical Review E* (1995) **52**, No. December, 6387.
[10] Patzek, T. W.: "Verification of a complete pore network simulator of drainage and imbibition," *SPE Journal* (2001) **6**, No. 2, 144–156.
[11] Al-Futaisi, A. and Patzek, T. W.: "Impact of Wettability on two-phase flow characteristics of sedimentary rock: Quasi-static model," *Water Resources Research* (2003) **39**, No. 2, 1042–1055.
[12] Patzek, T. W. and Silin, D. B.: "Shape Factor and Hydraulic Conductance in Noncircular Capillaries: I. One-Phase Creeping Flow," *Journal of Colloid and Interface Science* (April 2001) **236**, 295–304.
[13] Patzek, T. W. and Kristensen, J. G.: "Shape Factor and Hydraulic Conductance in Noncircular Capillaries: II. Two-Phase Creeping Flow," *Journal of Colloid and Interface Science* (April 2001) **236**, 305–317.
[14] Avkhadiev, F. G. and Kacimov, A. R.: "Analytical Solutions and Estimates for Microlevel Flows," *Journal of Porous Media* (2005) **8**, No. 2, 125–148.
[15] Entov, V. M.: "The micromechanics of flow in porous media," *Soviet Academy Izvestia. Mechanics of Gas and Fluids* (1992) No. 6, 90–102.
[16] Blunt, M. J.: "Flow in porous media - pore-network models and multiphase flow," *Current Opinion in Colloid & Interface Science* (2001) **6**, No. 3, 197–207.
[17] Martys, N. S. and Chen, H.: "Simulation of multicomponent fluids in complex three-dimensional geometries by the lattice Boltzmann method," *Physical Review E* (1996) **53**, 743.
[18] Auzerais, F. M., Dunsmuir, J., Ferreol, B. B., Martys, N., Olson, J., Ramakrishnan, T. S., Rothman, D. H., and Schwartz, L. M.: "Transport in sandstone: A study based on three dimensional microtomography," *Geophysycal Research Letters* (1996) **23**, 705–708.
[19] O'Connor, R. M. and Fredrich, J. T.: "Microscale flow modelling in geologic materials," *Physics and Chemistry of the Earth, Part A: Solid Earth and Geodesy* (1999) **24**, No. 7, 611–616.
[20] Fredrich, J. T., , DiGiovanni, A. A., and D. R. Noble, D. R.: "Predicting macroscopic transport properties using microscopic image data," *Journal of Geophysical Research* (2006) **111**, B03201.
[21] Jin, G., Patzek, T., and Silin, D. B.: "Direct Prediction of the Absolute Permeability of Unconsolidated and Consolidated Reservoir Rock. SPE 90084," 2003 SPE Annual Technical Conference and Exhibition, SPE, Houston, Texas, U.S.A. (2004).
[22] Noble, D. R., Chen, S., Georgiadis, J. G., and Buckius, R. O.: "A consistent hydrodynamic boundary condition for the lattice Boltzmann method," *Physics of Fluids* (1995) **7**, No. 1, 203–209.
[23] van Genabeek, O. and H., R. D.: "Macroscopic Manifestations of Microscopic Flows Through Porous Media," *Annual Review of Earth and Planetary Sciences* (May 1996) **24**, 63–87.
[24] d'Humières, D. and Ginzburg, I.: "Viscosity independent numerical errors for Lattice Boltzmann models: From recurrence equations to "magic" collision numbers," Computers and Mathematics with Applications; doi:10.1016/j.camwa.2009.02.008.
[25] Adler, P. M.: "Fractal porous media III: Transversal Stokes flow through random and Sierpinski carpets," *Transport in Porous Media* (April 1988) **3**, No. 2, 185–198.
[26] Schwartz, L. M., Martys, N., Bentz, D. P., Garboczi, E. J., and Torquato, S.: "Cross-property relations and permeability estimation in model porous media," *Physical Review E* (December 1993) **48**, No. 6, 4584 – 4591.
[27] Manwart, C., Aaltosalmi, U., Koponen, A., Hilfer, R., and Timonen, J.: "Lattice-Boltzmann and finite-difference simulations for the three-dimensional porous media," *Physical Review E* (2002) **66**, 016702 1–11.
[28] Manwart, C. and Hilfer, R.: "Numetrical simulations of creeping fluid flow in reconstruction models of porous media," *Physica A* (2002) **314**, 706–713.
[29] Silin, D. B., Jin, G., and Patzek, T. W.: "Robust deteremination of the pore-space morphology in sedimentary rocks," *Journal of Petroleum Technology* (May 2004) 69–70.
[30] Silin, D. B., Jin, G., and Patzek, T.: "Robust Determination of the Pore-Space Morphology in Sedimentary Rocks. SPE 84296," 2003 SPE Annual Technical Conference and Exhibition, SPE, Denver, Colorado, U.S.A. (2003).
[31] Silin, D. B. and Patzek, T. W.: "Pore space morphology analysis using maximal inscribed spheres," *Physica A. Statistical Mechanics and its Applications* (2006) **371**, 336–360.
[32] Silin, D. B. and Patzek, T. W.: "An Object-Oriented Cluster Search Algorithm," No. LBNL-51599, Lawrence Berkeley National Laboratory (2003).
[33] He, X., Doolen, G. D., and Clark, T.: "Comparison of the Lattice Boltzmann Method and the Artificial Compressibility Method for Navier-Stokes Equations," *Journal of Computational Physics* (July 2002) **179**, No. 2, 439–451.

[34] Chorin, A. J.: "A numerical method for solving incompressible viscous flow problems," *Journal of Computational Physics* (1967) **2**, 12–26.
[35] Tomutsa, L., Silin, D., and Radmilovic, V.: "Analysis of Chalk Petrophysical Properties By Means of Submicron-Scale Pore Imaging and Modeling," *SPE Reservoir Evaluation and Engineering* (June 2007) **10**, No. 3, 285–293.
[36] Benson, S. M., Tomutsa, L., Silin, D., Kneafsey, T., and Miljkovic, L.: "Core scale and pore scale studies of carbon dioxide migration in saline formations.," 8th International Conference on Greenhouse Gas Control Technologies. Trondheim, Norway, 19-22 June 2006. (2006).
[37] Landau, L. D. and Lifschitz, E. M.: *Fluid mechanics*, Series in advanced physics Series, Addison-Wesley, Reading, MA (1959) **6**.
[38] Chorin, A. J.: "Numerical solution of the Navier–Stokes equations," *Math. Comp.* (1968) **22**, 745–762.
[39] Harlow, F. and Welsh, J.: "Numerical calculation of time dependent viscous incommpressible flow with free surface," *Physics and Fluids* (1965) **8**, 2182–2189.
[40] Samarskii, A. A.: *The theory of difference schemes*, M. Decker, New York (2001).
[41] Wyckoff, R. T. and Botset, H. G.: "The Flow of Gas-Liquid Mixtures through Unconsolidated Sands," (September 1936) **7**, 325–345.
[42] Muskat, M. and Meres, M. W.: "The Flow of Hetereogeneous Fluids Through Porous Media," (September 1936) **7**, 346–363.
[43] Leverett, M. C.: "Flow of Oil-water Mixtures through Unconsolidated Sands," *Trans. AIME* (1939) **132**, 381–401.
[44] Finney, J. L.: "Random packings and the structure of simple liquids. I. The geometry of random close packing," *Proceedings of the Royal Society of London. Series A* (1970) **319**, No. 1539, 479–493.
[45] Bourblaux, B. J. and Kalaydjian, F. J.: "Experimental Study of Cocurrent and Countercurrent Flows in Natural Porous Media," *SPE Reservoir Engineering* (August 1990) **4**, 361–368.
[46] Ransohoff, T. C. and Radke, C. J.: "Laminar flow of a wetting liquid along corners of a predominantly gas-occupied noncircular pore," *Journal of Colloid and Interface Science* (1998) **121**, 392–401.
[47] Anderson, W. G.: "Wettability Literature Survey– Part 4: Effects of Wettability on Capillary Pressure," *Journal of Petroleum Technology* (October 1987) **39**, No. 10, 1283–1300.